New SPIS capabilities to simulate dust electrostatic charging, transport and contamination of lunar probes

S.L.G. Hess, P. Sarrailh, J.-C. Matéo-Vélez, B. Jeanty-Ruard, F. Cipriani, J. Forest, A. Hilgers, F. Honary, B. Thiébault, S.R. Marple and D. Rodgers

***Abstract*—The Spacecraft Plasma interaction Software (SPIS) has been improved to allow for the simulation of lunar and asteroid dust emission, transport, deposition and interaction with a spacecraft on or close to the lunar surface. The physics of dust charging and of the forces that they are subject to has been carefully implemented in the code. It is both a tool to address the risks faced by lunar probes on the surface, and a tool to study the dust transport physics. We hereby present the details of the physics that has been implemented in the code, as well as the interface improvements that allow for a user friendly insertion of the lunar topology and of the lander in the simulation domain. A realistic case is presented that highlights the capabilities of the code as well as some general results about the interaction between a probe and a dusty environment.**

***Index Terms* — Electrostatic levitation, Lunar dust, Surface charging.**

I. INTRODUCTION

The Apollo missions demonstrated that the lunar regolith, composed of very small dust particles of micron to sub-micron sizes, is a potential threat to any mission on or close to the moon surface (see review by [1]). The lunar dust particles are highly adhesive due to their small size and their electrostatic charge. These dust particless are also highly abrasive, so that friction with surfaces can wear down materials and reduce material lifetimes. Dust also pose a potential health hazard to astronauts.

The electrostatic charging of the lunar dust grains is suspected to be a key ingredient of the observation of dust "levitation" above the lunar surface and of the formation of a dust haze that may extend to several tens of kilometers in altitude [2][3][4]. The dust ejection from the ground and subsequent motion is though to be due to a combination of factors including micro-meteorite impacts and electrostatic forces. The latter is expected to be amplified by the lighting variation on the irregular moon surface, in particular close to the crater rims. The ejected dust particles can be deposited on landers on the moon surface.

To investigate for potential lunar mission risks, the capabilities of the Spacecraft-Plasma Interaction Simulator (SPIS) were extended to include the modeling of the lunar dust charging, ejection, dynamics in the plasma and deposition on surfaces in the frame of an ESA contract (SPIS-DUST). The present paper details the extension to SPIS, both from a practical (inputs from the user interface) and theoretical (numerical modeling) point of views. The User Interface now permits one to build a simulation geometry based on Lunar topological data and to include a lander in it, and the numerical core was extended to handle the physics of dust particle charging and a better description of the plasma sheath above the ground. The user interface and the numerical core have also been extended to allow for the use of new diagnosis instruments related to the dust particle motion and characteristics in and out of the simulation domain.

The model we present is an improvement compared to previously published models of the dust spacecraft interactions on the lunar surface [5] as it improves the dust charging computation by taking into account the secondary electron emission from the dust particles, and the dust transport by taking into account the photon pressure on the dust grains. Moreover, contrary to the precedent models we implemented a model of the dust charging on the ground and of the dust ejection which takes into account the charge distribution between the dusts, the cohesive and seismic forces.

In section II, we present the set up of the simulation with the User Interface. The numerical methods that are used to build the simulation domain from topological data and the observational data that are used are presented. Section III discusses the physical models of the plasma sheath and of the dust charging and dynamics in the volume and on surface. An early study of these processes including a preliminary implementation of some of them can be found in [6], which concentrates on determining the important phenomena intervening in the dust dynamics and how to implement them. The present study concentrates on the final, operational implementation of the dust particle dynamics in SPIS. A test case of the interaction between a lander and the lunar dust is presented in section IV.

The present study and the modifications to the Spacecraft Plasma Interaction Software have been undertaken under ESA contract 4000107327/12/NL/AK (SPIS-DUST).

S.L.G. Hess, P. Sarrailh, J.-C. Matéo-Vélez and are with ONERA - The French Aerospace Lab, Toulouse, France (e-mail: sebastien.hess@onera.fr)

F. Cipriani, D. Rodgers and A. Hilgers are with the ESA/ESTEC, Noordwijk, The Netherlands

B. Jeanty-Ruard, B. Thiébault and J. Forest are with Artenum, Paris, France

F. Honary and S. Marple are with the University of Lancaster, Department of Physics, Lancaster, United-Kingdom

II. Defining a Simulation of the Dusty Lunar Surface with User Interface

A. Geometry definition

In order to ease studies targeting a precise site on the moon, it is possible to generate the SPIS simulation domain directly from a set of "geographical" 3D coordinates of the lunar surface or elevation points. It is performed in five steps, the first four define the lunar surface geometry (Figure 2), and the last one defines the computational volume by extrusion of the surface border.

After the list of coordinates is loaded in SPIS (Step 1), the boundary of the 2D surface is automatically computed by SPIS (Step 2). The border identification is based on the Gift Wrapping Algorithm [7]. It starts with the point P_0 in the list with the minimal abscissa and then iteratively searches for the neighboring point on the border. To identify the second point on the boundary, P_1,, one searches for P_1 so that the angle between the $[P_0,P_1]$ segment and a straight line *d* passing by P_0 and parallel to the ordinate axis is minimal. The next point on the boundary than corresponds to the point P_2 presenting the minimal angle $\widehat{P_0P_1P_2}$. Figure 1 presents this iterative algorithm, called the Gift Wrapping Algorithm. The points P_3', P_3'' and P_3''' are different possible choices for the next point on the boundary after the selection of point. As $\widehat{P_1P_2P_3'} > \widehat{P_1P_2P_3''} > \widehat{P_1P_2P_3'''}$, the point P_3''' is selected. The implemented algorithm performance is fully acceptable for the targeted configurations, but it is possible to compute a rectangular border as an alternative.

Then, the surface is meshed as a planar surface using the Gmsh mesher (Step 3) and, the elevation of the surface is computed in an operation called kriging[8][9][10] (Step 4). The kriging method starts with the selection of the neighboring points of the node x_0, whose altitude has to be computed. The neighboring points are extracted from the set of elevation points of the lunar surface. The space around the node is divided in four quadrants, with a user-defined selection radius R_s, in which a given maximum number of neighbors will be searched for. If no neighbor is found, the node x_0 is removed from the mesh. However in this case, the output mesh will present a hole and will not be consistent. To address this issue, several solutions may be considered.

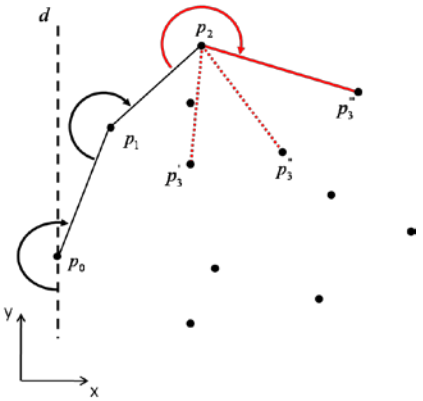

Figure 1: Illustration of Gift Wrapping Algorithm

First, the user can edit manually the mesh and add an additional vertex and connect it with the rest of the mesh. Second, the user may add extra elevation points at the vicinity of the targeted mesh point. Third, it is possible to increase R_s in order to select at least one neighbor elevation point. In the general case, it recommended to check that the elevation points of the lunar surface are denser than the local characteristic size of the mesh elements. The kriging interpolation of the altitude z_0^* of the point x_0 is:

$$z_0^* = Z^t K^{-1} K_0. \quad (1)$$

The components of the covariance matrix **K** correspond to covariance factors, function of the distance between the neighbor points x_i and x_j. The components of the covariance vector $\mathbf{K_0}$ correspond to covariance factors, function of the distance between the points x_i and x_0. The altitude vector **Z** components correspond to the elevations of the neighboring points x_i. The ground tessellation is able to generate a mesh with 600 elements from about 10^5 ground coordinates in about 15 seconds on a standard desktop PC. However, some parts of the algorithm are non-linear, so that large systems must be considered with care.

B. Lander insertion

The insertion of a lander in the simulation implies to apply a careful processing of the interface between the lander and the surface meshes. An algorithm implemented in SPIS detects the N closest pairs (i.e. with closest barycenters) of lunar and spacecraft surfaces (N is set by the user). The user is given the possibility to select which pairs are merged. New faces are created that links the lander to the ground.

C. Definition of the material properties

SPIS predefined materials did not include material approaching that of the lunar surface, so new dusty materials have been added to the SPIS material list. The main property of this material is the distribution of the dust particle sizes. The dust particle size distribution is taken from [11], p306, referred as 71501,1 Mare. The original plot did not clearly present particles of radii lower than 1 µm. As a result, we extrapolated for radii smaller than 1µm a radius distribution function of the form $f(r) = A.r^2\exp(-B.r^2)$, shown on Figure 3.

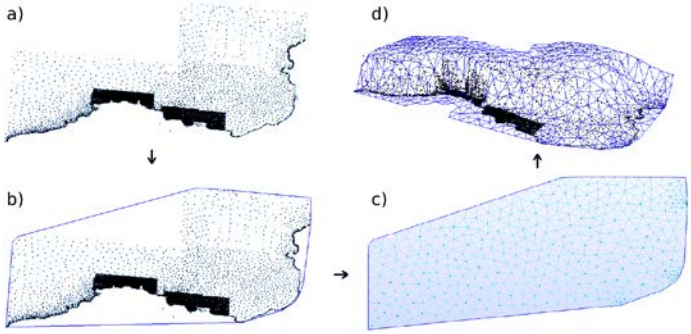

Figure 2: Steps for the definition of the lunar surface mesh from a list of ground coordinates: (a) the coordinates of points on the surface are loaded, (b) the contour of simulation domain is computed, (c) the surface is meshed as a flat surface and (d) the node altitudes are computed by a kriging method.

The conductivity of lunar dust varies considerably between the samples returned back from Apollo missions. From [11], the bulk conductivities of Apollo 15 soil (15301,38) and Apollo 16 rock (65015,6) depend on the temperature. In addition, [11] reports that UV illumination increases the conductivity of soils by a factor 10^6, comparable to that produced by a temperature of 800°C. We defined a resistive lunar surface material with an arbitrary low bulk conductivity of 10^{-18} $\Omega^{-1}.m^{-1}$ and a large surface resistivity of 10^{18} Ω, and a conductive one (with infinite bulk and surface conductivities) corresponding to shadowed and sunlit surfaces, respectively.

The lunar material current density at normal sunlight incidence angle is J_{p0} = 4.5 μA/m^2 at 1 AU for lunar dust [12]. The secondary emission from particle impact [12] is assumed to be low at the surface, but the secondary emission model of [13] is implemented for the emission induced by electron impact in the volume. This model depends on the inverse of the energy required to excite a single secondary electron (K = 0.01 eV^{-1}), the inverse of the absorption length for secondary electrons ($\alpha = 10^8$ m^{-1}), and the Whiddington constant for the rate loss with distance (a = 10^{14} V^2.m^{-1}).

III. Physical Modeling

A. Plasma sheath

The simulation domain does not cover the Moon entirely, it rather is a box with an open face through which the solar wind plasma is injected, a lunar surface face absorbing the solar wind plasma and emitting photo-electrons and dust particles, and lateral boundaries either reflecting or periodic. The dimension of the system is thus closer to 1D than to 3D, as no current divergence can exist across the side boundaries. In this configuration, the quasi-neutrality of the plasma at the open boundary (figuring the undisturbed solar wind) is not ensured: A negative sheath potential repels part of the solar wind electrons but none of the solar wind ions, resulting in different densities across the simulation domain, including at the open boundary. Moreover, some photo-electrons emitted from the surface reach the open-boundary. In a 3D case, the neutrality would be enforced by a divergence of the incoming solar wind electron flux and of the outgoing photo-electron flux, but in a 1D case the quasi-neutrality has to be imposed by a careful determination of the boundary conditions [15][16].

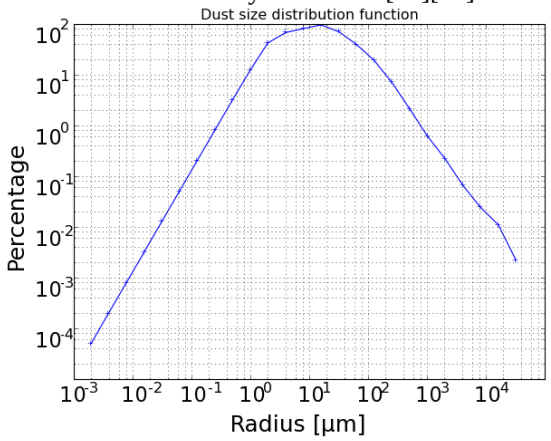

Figure 3 : Distribution of the dust particle radii (m) used in SPIS from fit of the table given in [11].

SPIS adjusts automatically the influx of solar wind electrons to ensure quasi-neutrality at the open boundary. The computation is based on the motion of the different populations along a potential profile such as that found by [14] (Panel a of Figure 4). The detail of the sheath modelling and calculations can be found in a dedicated paper [16], which also discuss the effects of the surface topology and of the solar wind parameters on the surface and sheath potential profile.

Since the ion bulk velocity is larger than their thermal velocity and large enough to overcome the electric potential effects, the ion density is constant in the domain. The photoelectron density at the open boundary, $v_{p\infty}$, is obtained from the photoelectron current and velocity at this point. The velocity is estimated from the photoelectron thermal and potential energies at the peak of the sheath potential barrier. For a Maxwellian distribution it is approximately:

$$v_{p\infty} \sim \sqrt{\frac{\frac{2}{\pi} kT_{p-2eV_{dip}}}{m_e}}, \quad (2)$$

with -e, m_e and T_p the photoelectron charge, mass and temperature, respectively. V_{dip} is the most negative potential.

The current at the open-boundary is taken equal to that at the peak of the potential barrier and is estimated from the current emitted by the surface and the potential difference across the sheath. The surface material current density at normal sunlight incidence angle, J_{p0}, is modulated by the solar inclination relative to the normal to the surface. For non-planar surfaces, the current computation only takes into account the fraction of photoelectron distribution corresponding to electron emitted toward positive altitudes. The current density, J_{pi}, emitted by the ith surface element is [16]:

$$J_{pi} = J_{p0} S_i (\vec{\varphi}.\vec{n})(1 - \pi^{-1} acos(\vec{n}.\langle\vec{n}\rangle)). \quad (3)$$

where S_i is the shadowing transfer function (equal to the fraction of the surface elements which receive direct lighting from the open boundary) and $(\vec{\varphi}.\vec{n})$ is the geometrical term taking into account the angle between the sun direction, $\vec{\varphi}$, and the normal to the surface element, $\vec{n}$. $\left(1 - \pi^{-1} acos(\vec{n}.\langle\vec{n}\rangle)\right)$ is the fraction of the velocity distribution function corresponding to positive velocities in the direction normal to the average plane of the surface, $\langle\vec{n}\rangle$.

The current density at the peak of the potential barrier is that emitted at the surface, J_{pi}, minus the recollection, which depends on the difference between the surface potential, V_{surf}, and the barrier potential, V_{dip}, and on the photo-electron distribution function. Dielectric surfaces introduce a difference between the local surface potential and the potential averaged on the whole surface, $\langle V_{surf}\rangle$, resulting in a misalignment of the distribution function which can be estimated from the ratio of the potential and kinetic energies. For a Maxwellian distribution, the current at the open boundary coming from the ith surface element (of area σ_i) is [16]:

$$I_i = J_{pi}\sigma_i exp\left(\frac{-\max\left(0, e\left(V_{surf} - V_{dip}\right)\right)}{kT_p}\right)$$
$$\left(1 - \pi^{-1} \operatorname{atan}\left(\frac{\min\left(0, e\left(V_{surf} - \langle V_{surf}\rangle\right)\right)}{m\langle\vec{v}.\vec{n}\rangle^2}\right)\right) \quad (4)$$

The exponential term stand for the recollection of the dust whose energy is not sufficient to pass the potential barrier. The last term account for the misalignment of the distribution relative to the local normal to the surface due to the differential charging of the surface.

For non-Maxwellian distributions, this term is evaluated numerically. The density of photo-electrons at the open boundary is the sum of the currents emitted by each surface element divided by the electrons charge, by velocity at the open boundary and by the potential barrier cross section, A.

$$n_{p\infty} = \frac{\sum_{i \in surface} J_i}{-e v_{p\infty} A}. \quad (5)$$

Because the solar wind electron thermal velocity is larger than their bulk velocity and because their kinetic energy is of the same order of the potential energy, the solar wind electron distribution at the open boundary is not Maxwellian: even though the down-going electrons have a drifting Maxwellian distribution, the up-going have not. Hence, the solar wind electron density at the open boundary, n_e, is not that of the drifting Maxwellian population incoming from the solar wind, n_{e0}. Assuming a Maxwellian distribution, the solar wind electron density at the open boundary is:

$$n_e = n_i - n_{p\infty} = \frac{n_{e0}}{2}\left(1 + 2\,\mathrm{erf}\left(\frac{v_d}{v_{Te}}\right) - \mathrm{erf}\left(\frac{v_d}{v_{Te}} - \sqrt{\frac{eV_{dip}}{kT_e}}\right)\right). \quad (6)$$

v_d is the bulk velocity of the solar wind and the thermal velocity is $v_{Te} = \sqrt{(2kT_e)/m_e}$. SPIS determines the density of the Maxwellian population, n_{e0}, to inject in the simulation.

Panels a and b of Figure 4 show the electric potential and the density profiles for the test case, respectively. The difference between the results of [14] and ours are due to slightly different boundary conditions, different solar zenith angles and the presence of a crater in our simulation. The profile is computed along a line passing through the crater center.

Indeed, the above equation is only a first order approximation of the injected electron flux. Thus, the quasi-neutrality is not perfectly enforced at the open boundary, but still strongly enhanced compared to simulations without the correction of the electron influx (Panel a of Figure 4).

B. *Dust emission*

1) *Dust distribution at the surface*

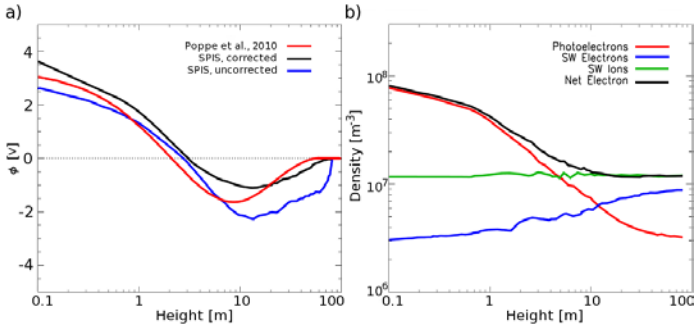

Figure 4: (a) Potential profiles for the simulation of [14] (red) and the test case with (black) and without (blue) the correction of the solar wind electron influx. (b) Density profiles for the test case with the electron influx correction.

Dust is automatically emitted from a surface if the surface material has dust properties (i.e. at least a dust radius distribution function). The first step of the interaction computation is the conversion of the distribution function of the dust particles in radius, mass and shape into a macroparticle list sampling the particles on the lunar surface.

The sampling of the particle distribution function in an equiprobable way (i.e. all the macroparticles have the same statistical weight and represent the same number of physical dusts) is not optimal in most of the cases as the radii of the dusts that are able to takeoff are not that of the most numerous ones on the surface. Computationally, it is more efficient to sample more small dust particles (with radius less than 1µm) than larger ones that stick on the lunar surface due to the gravity. A parameter of SPIS controls of the macroparticle sampling probability to favor the lighter dust particles.

The surface density computed by SPIS from the distributions provided by data from the literature [11] is:

$$n_s = \frac{\sum_{i=0}^{N} w_i}{\sum_{i=0}^{N} \pi r^2 w_i}, \quad (9)$$

where w_i is the statistical weight of the i^{th} macroparticle and N is the number of macroparticles on the surface. The effective charged surface area can be larger than the smooth geometrical surface area, which is not unphysical as the actual lunar surface roughness must be taken into account.

2) *Dust charging on the surface*

The global charge of a surface element is computed from the Gauss's law – given the electric field on the surface – to have a total charge consistent with the sheath.

$$Q_i = \varepsilon_0 E_i \sigma_i, \quad (10)$$

Q_i and E_i being the charge and electric field on the i^{th} surface element, respectively. The electric field is updated at each time step from the Poisson equation, bounded by the fixed potential at the open boundary and by the surface potential computed by solving the surface equivalent circuit. The charge distribution in depth is unknown for a soil composed of dust particles as no model of the charging of a granular material in space condition was ever published. We assume that the charge is carried by the uppermost layer of dust particles.

Between two iterations (time steps), the variation of the surface charge, ΔQ_i, is computed and the charge difference is distributed between all the dust on the surface as a function of their radius. The charges of the dusts depend linearly on their radius, r_d, as the potentials of the dust particles are considered to be the surface potential and as the dust capacitance is assumed to be that of a sphere. Thus, the charge variation on the surface is distributed between the macroparticles such as

$$\Delta Q_D \sim r_d \times \Delta Q_i, \quad (11)$$

$$\sum_N w\, \Delta Q_D = \Delta Q_i\ . \quad (12)$$

For dust particles on the ground, the charging current is not an OML current like for the charging in volume but it implies currents between particles. We assume that the charging time for the dust particles on the ground is the smaller of the isolated particle (OML) charging time or of the charging time

of dust particles represented as RC components of an electrical circuit. Assuming typical solar wind parameters, OML charging times is of many thousands of seconds. Assuming a dust particle resistivity of ρ=10^9 Ω.m [10], the RC circuit charging time, $\epsilon_0\rho$, is about 0.01s, i.e. five orders of magnitude shorter. Even considering that the actual resistivity may be larger between dust particles, the conductivity between the grains would still be the primary source of charging for the dust particles on the ground. Resistivity of 10^{11} Ω.m has been found for dusty material in low density neutral environments [17], but it is more conductive in plasma environment due to the larger amount of free charges between the dust grains.

The charge for a micron sized dust is 10^{-4}e assuming a typical electric field of 2V/m like that found in our simulation. Thus the charges are not evenly distributed among the dusts. In SPIS, we model this uneven distribution using of an amplification factor by analogy the tip effect. We assume there are tips that have a radius r and a height L, separated from each other by a distance L. Then we have regions of field and charge enhancement by a factor β that cover a fraction β^{-2} of the surface. For the computation of the force balance on the surface, a secondary charge and weight are defined:

$$\Delta Q'_D = \beta\, \Delta Q_D \; and \; w' = \frac{w}{\beta^2}. \quad (13)$$

The sum of the charges, weighted by the macroparticle weights, are not the same whether we consider Q_D or Q'_D. The latter can be considered as being the average charge on surface of the dusts within the macroparticles that are ejected, whereas Q_D is the average charge on surface of all the dusts within the macroparticles. The actual value of β is determined for the force balance as discussed in the next section. This tip model is oversimplified, but is a first approximation to overcome the absence of dusty soil charging models so far.

3) Force balance on the surface dusts

SPIS takes into account several forces that apply to the dust particles on the surface:

The electrostatic force is computed from the projection of the electric field on the barycenter of the surface elements, the charge of the dusts and the field amplification factor due to local amplification structures.

$$\overrightarrow{F_E} = Q_D'\beta(\vec{E}.\vec{n})\vec{n} = Q_D\beta^2(\vec{E}.\vec{n})\vec{n}. \quad (14)$$

The amplification factor of the electric field has thus a huge influence on the electrostatic force as it appears in the electric field and in the dust charge (quadratic influence).

The gravity force is directly the product of the gravity vector projection on surface element and the mass of the dust grain:

$$\overrightarrow{F_G} = m_D(\vec{g}.\vec{n})\vec{n}. \quad (15)$$

The gravity force is zero where the surfaces are orthogonal to the gravity vector, causing some problems in comparison to the reality where the roughness of the surface prevents the gravity to be completely orthogonal to the local surface.

The Van der Waals force is modelled as

$$\overrightarrow{F_C} = -KS^2.r_D\vec{n}. \quad (16)$$

From the literature, the factor K is about 5e-2 kg/s^2 and S is about 0.8 [18][19]. According to [20], it seems impossible to launch particles submitted to such a force (1 µm size dusts undergo a 10^{-8} N force). As a result, the authors suggested that the dust cleanliness and the non-uniform charge could lead to a strong decrease of the cohesion force and to a strong increase of the electrostatic force, respectively. We thus consider that KS^2 is equal to 10^{-6} kg/s^2, following the recommendation of [14].

Seismic forces, $\overrightarrow{F_s}$, can also be included. They are defined by their 3D amplitudes, frequencies and phases.

To avoid the emission of dust particles which immediately fall back on the ground, the enhancement factor β is that for which the work due to the sum of the forces over the dust radius (about the distance over which the microscopic forces act) correspond to the kinetic energy of the dust moving at a velocity of 0.4 m.s^{-1} (i.e. particles reaching an altitude of 20 cm if no other forces than gravity act). The macroparticle is then ejected with the weight $w' = w\beta^{-2}$ and with an initial velocity of 0.4 m.s^{-1}. All enhancement factor $\beta > 1$ are possible but with a probability β^{-2} carried by the particle weight. Thus, the field amplification factor participates in the scaling of the emitted flux.

The rate at which the dusts are emitted is assumed to be limited by the charging time of the freshly uncovered dusts. The final weight of the emitted particle is thus:

$$w_{emit} = \frac{w}{\beta^2}\frac{\delta t}{\epsilon_0\rho}, \quad (17)$$

with δt the time step and ρ the resistivity of the dusts, taken in our simulation equal to 10^9 Ω.m following [10].

The ejected macroparticle charges are computed from the potential at the surface, $V_{surface}$, assuming a spherical capacitance and from the triboelectric charging:

$$Q_{D\_injected} = 4\pi\varepsilon_0 r_d V_{surface} + (Q_r r_d + Q_w)(W - W_d). \quad (18)$$

W and W_d are the surface material and dust work functions and Q_r and Q_w are parameters obtained from the linear fit of the measurements of [21].

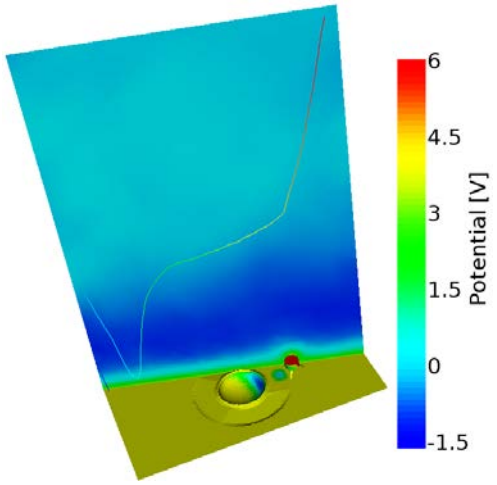

Figure 5: Electric potential on the surface and in the volume and a dust trajectory.

C. Dust dynamics

Once ejected, the dust dynamics is computed in a way similar to any other particle, the cohesive and seismic forces do not apply anymore, but the magnetic field and the photon pressure do. The electrostatic force is computed without the enhancement factor, as it results from local microscopic inhomogeneities in the field at the surface.

Nevertheless, the dust dynamics differ from that of the other particles due to the fact that its charge varies with time, both because of plasma collection on the dust particles and of secondary emission. The dust potential is computed considering a capacitive coupling following [22]:

$$V_d(t) = \frac{Q_D(t)}{4\pi\varepsilon_0 r_d(1+r_d/\lambda_D)}. \quad (19)$$

λ_D is the Debye length. From this potential, the collected current, J_c, is either computed from the OML model (fluid populations) and/or by a Monte Carlo scheme for PIC populations.

The secondary electron emission under electron impact is also computed (that from proton impact is neglected after [12]). The model of [13] is implemented. The electron yield depends on the primary electron energy and the dust radius. The dust particle potential acts on the secondary emission both through the primary electron collection and through the secondary electron energies. The net secondary electron emission (SEEE) current, J_s, is scaled by the potential difference between the dust and the plasma.

The total charge of the dust particles is updated at each time step following the current balance:

$$\frac{dQ_d}{dt} = J_c + J_s + J_p. \quad (20)$$

J_p is the photo-emission current. On the surface, the flux is moderated by the sun incidence angle (see section III.A). For dusts in the plasma, the photocurrent is either maximal when irradiated or zero when shaded by an element of surface. The dust photoelectron current is the multiplication of the photoelectron current density by the dust grain cross section.

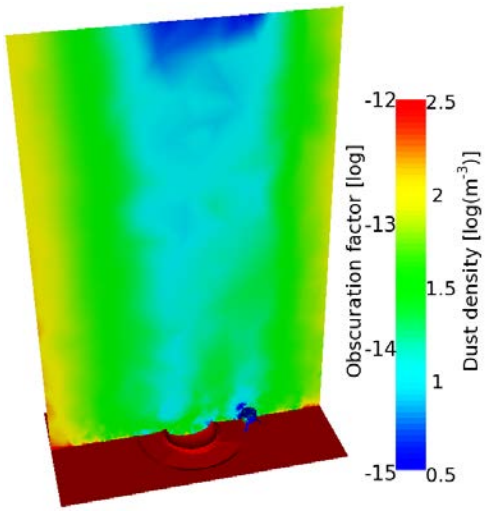

Figure 6 : Dust density on a simulation domain cut and the obscuration factor (fraction of the surfaces covered).

On the lunar surface, the velocity distribution function of photo-electron is Maxwellian by default, with a temperature of 2.2 eV, but a Feuerbacher distribution determined by [23] can also be used. For dust particles in the plasma, the Feuerbacher flux distribution is always used:

$$f_p(v) = \frac{4\varphi}{\Gamma\left(\frac{5}{4}\right)v_p^5} v^4 exp\left[-\left(\frac{v}{v_p}\right)^4\right]. \quad (21)$$

where φ is the total flux of photoelectrons on a surface element (in $m^{-2}.s^{-1}$) or in volume for dust in the plasma (in $m^{-3}.s^{-1}$). As for the SEEE, the net current emitted depends on the potential difference between the dust and the plasma, ΔV. The photoelectron current from the dust particles in the plasma (recollection being accounted for) is estimated as:

$$I_p = J_p \pi r^2 exp\left(-\frac{\max(0,e\Delta V)}{kT_p}\right). \quad (22)$$

This estimate is exact for a Maxwellian population but is only a first order approximation for a Feuerbacher distribution.

IV. Simulation of a Lander in a Crater Vicinity

Several test cases were run during the SPIS-DUST development. In the present paper, we present a single example of a case representing a small lander located close to a crater on the lunar surface, while the moon is in the solar wind. The crater has a radius of 5 meter and a depth of 2 meters and is surrounded by a 0.5 meter wide rim. The simulation domain is rectangular, with a 54m×27m cross section. The boundary conditions on the smaller lateral surfaces are periodic to allow for an inclined solar wind direction and that on the larger lateral surfaces are reflective. The electric field is fixed to 0V/m on all lateral surfaces.

The lunar surface outside the crater is conductive, as no obstacle may shade on it, whereas the surface inside the crater, including its rim, is dielectric (we do not precisely separate shaded and lighted surfaces in this simulation).

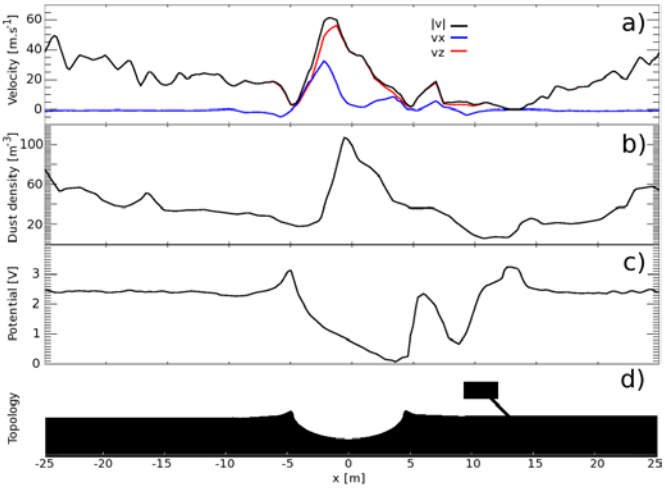

Figure 7: (a) Dust velocity shown in terms of absolute, parallel and normal velocities relative to the ground, (b) dust density and (c) electric potential along a line passing through the middle of the crater and 0.6 m above the ground. At the bottom of the figure (d), the surface topology is shown with the lander and one of its three legs.

The surface between the crater and the lander is also dielectric as the lander itself creates a shadow on the ground. As the sunlight incidence angle is 45° in the simulation, the surface of the crater charges differentially.

The solar wind density is n_i = 10 cm^{-3} for ion and automatically scaled to n_{e0} ~ 9.1 cm^{-3} by SPIS for the electrons, with equal temperatures of 10 eV for both species. Both populations have a bulk velocity of 400 km/s opposite to the sun direction (inclined by 45° in the XZ plane). The potential is fixed to 0V at the open boundary. The spacecraft is modeled as a 3 meter wide, 1.5 m high cylinder mounted on three 2 m long "legs" inclined by 45°. The cylinder top and bottom are covered with Kapton, the legs are made of aluminum and the cylinder walls are made of cover glass.

The simulation is performed with a 2.2 eV Maxwellian distribution of photo-electrons. Since SPIS only allows the definition of a single photo-electrons distribution function for all of the surfaces in the simulation, it was not possible to assign a Feuerbacher distribution to the photo-electrons coming from the lunar surface and a Maxwellian one to those coming from the spacecraft. The simulation runs until it reaches a stationary state (here representing 50 seconds).

Figure 5 shows the electric potential on surface and in the volume and the trajectory of a dust grain emitted close to the lander. The most negative regions on the surface correspond to the shadowed lunar surfaces, whereas the lander feet charge positively. The negative potential barrier is visible a few meters above the surface. It is thick enough so that it hides the spatial differences that exist below it, and offers quasi-one dimensional conditions above it. This allows our computation of the solar wind electron influx to be consistent.

Dust particles are mainly emitted from positive surfaces and charge positively in the volume by secondary and photo-emission of electrons. This can be tracked by a dust trajectory sensor included in SPIS. The charge, velocity and potential of the test particles are monitored in the User Interface.

Most of the dusts fall back due to gravity, but some of falling dusts (lighter and more charged) are reflected by the positive potential of the lunar ground. This leads to a trapping of the dusts in the negative potential barrier due to the photo-electron sheath at a few meters above the ground. The lightest and most charged dusts are then lost through the open boundary.

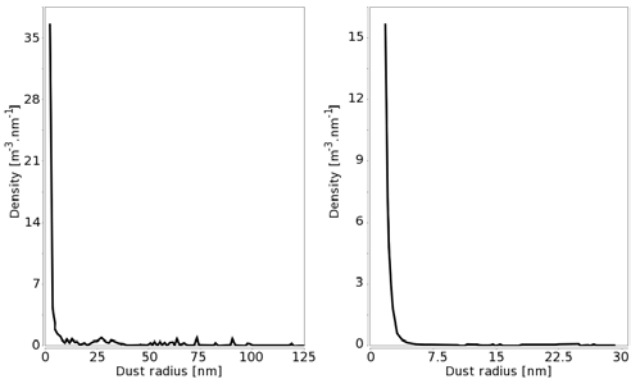

Figure 8: Dust size distributions inside the crater and close to the open boundary, above the crater center.

Figure 6 shows a cut of the dust density in the simulation domain and the dust "obscuration factor", i.e. the fraction of the surface covered by dusts. The dust density is lower above the crater than above the flat surface, in particular close to the sunlit rim although it is the preferential region of dust emission. This is actually due to the larger velocities of the dusts in these regions.

This can be seen on Figure 7, which shows the dust velocity parallel, V_x, and normal, V_z, to the ground, the dust density and the electric potential 0.6 m above the ground. The velocity in the sunlit part of the crater is much larger than on the shadowed one, and directed upward whereas on the shadowed part the velocity falls to almost zero and is downward (re-deposition) for dust larger than a few tens of nanometers.

The dust particles are accelerated from the sunlit parts to the shadowed ones. Indeed, the dust density is larger where the dust deposits than where they are emitted with a fast velocity. The dust density profile shows depletion close to the sunlit edge, a larger density above the crater center. Our results are consistent with the scenario of [24]: a dust emission from the sunlit edge of the crater with a re-deposition on dust over the whole crater, which in the end leads to dust depletions on the crater borders and a dust concentration in the crater center.

The obscuration factor map on Figure 6 shows that the dust preferentially deposits on the shadowed part of the spacecraft, which is negatively charged. This is easily understandable, as levitating dust particles are mostly positively charged.

Figure 8 shows the dust radius distributions in the crater and close to the open boundary. These distributions are computed by a new SPIS-DUST diagnostic tool, which permits one to monitor the dust particles inside a spherical volume. The dust individual properties, their distributions and their mean values are computed and can be displayed. This tool shows that dust grains larger than a 0.1 micrometer that may be emitted from the ground do not reach altitudes larger than a few meters.

Figure 9 shows the density of dust as a function of the altitude and radius above the simulation box. This distribution is determined by SPIS-DUST, which computes the trajectories of the dust particles crossing the open boundary, assuming that their charge does not evolve out of the simulation domain.

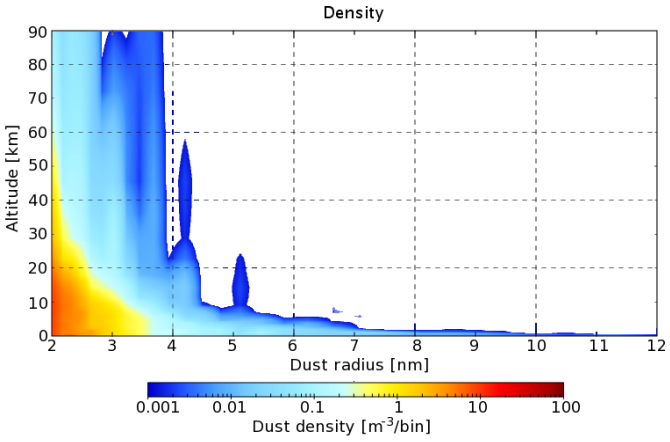

Figure 9: Density of dust above the simulation domain, as a function of altitude and dust radius.

The radial acceleration of the dust particles depends on the inertial term (that is on their tangential velocity v_θ), on the gravity (given by the gravitational acceleration at the surface g) and on the electrostatic force over a Debye length λ_D:

$$\frac{d^2z}{dt^2} = \frac{v_\theta^2 - gR}{z+R} + \frac{Q_d}{m_d} E_z e^{-z/\lambda_D} \quad (23)$$

z is the altitude relative to the surface and R is the Moon radius. From these trajectories the density of dust as a function of altitude and of the dust radii is computed. Nanometer dust particles can reach several tens of kilometers, whereas dust particles larger than 0.01 µm do not cross the open boundary (80 m of altitude), in accordance with the results of [25].

Figure 10 shows the density profile integrated over the dust radii. The corresponding column density is found to be about 100 cm^{-2}. It is to be compared with the high altitude dust profiles, or model of dust exospheres, which have been published [3][4]. These models consider much larger dust particles (~0.1µm) and find densities which can be either consistent (although larger) [4] or several orders of magnitude larger [3] than our results. Our results are not necessarily in contradiction with these studies as they are models constrained by exosphere remote observations (not directly related to the surface processes) and since our study is a simple test case with a first order extrapolation of the dust densities at high altitude. These discrepancies can be addressed in more detailed studies using the SPIS capabilities we developed.

V. Summary

The Spacecraft Plasma Interaction Software (SPIS) has been further developed to simulate the physics of the dust charging and transport above the lunar surface. This includes a description of the interaction between the dust and spacecraft with the implementation of the triboelectric effect. SPIS now permits one to address the risks for a lander on celestial bodies without atmosphere such as the moon and asteroids. A tool for computing a risk matrix has been included for this purpose that takes into account user specified material hardness, severity of abrasion and failure risk for the mission as well as the computed impact rate. SPIS also offers the possibility to investigate the physics of the dust charging and transport in the astrophysical plasmas from a scientific perspective, allowing a better understanding of the dusty environments of the astronomical bodies.

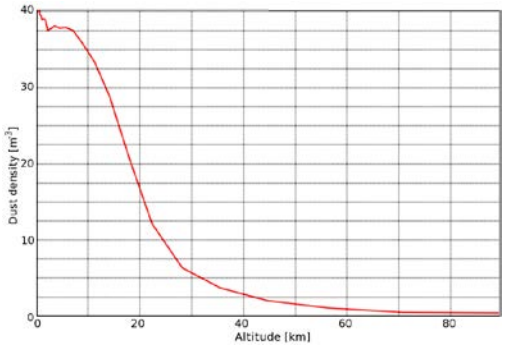

Figure 10 : Dust density profile versus altitude extrapolated above the simulation domain up to 90km.

References

[1] B.J. O'Brien, "Review of measurements of dust movements on the Moon during Apollo", Planetary and Space Science, 59, p. 1708-1726, 2011

[2] D.R. Criswell, "Lunar dust motion", Geochim. Cosmochim. Acta., Suppl. 3, p. 2671-2680, 1972.

[3] J.J. Rennilson, D.R. Criswell, "Surveyor observations of lunar horizon glow", earth Moon planet, 10, p 121-142, 1974.

[4] P.D. Feldman, D.A. Glenar, T.J. Stubbs, K.D. Retherford, G.R. Gladstone, P.F. Miles, D.E. Greathouse, J.W. Parker, S.A. Stern, "Upper limits for lunar dust exosphere from far-ultraviolet spectroscopy by LRO/LAMP", Icarus, 233, p 106-113, 2014.

[5] J. Wang, X. He, Y. Cao, "Modeling Spacecraft Charging and Charged Dust Particle Interactions on Lunar surface", 10th Spacecraft Charging Technology Conference, IEEE Transaction on plasma science, 36, 2008

[6] A. K. Anuar, F. Honary, M. Hapgood, J.-F. Roussel, "Three-dimensional simulation of dust charging and dusty plasma using SPIS", J. Geophys. Res. , 118, 6723–6735, 2013

[7] R. A. Jarvis, "On the identification of the convex hull of a finite set of points in the plane". Information Processing Letters 2, 18–21,1973.

[8] P. Bailly du Bois, "Automatic calculation of bathymetry for coastal hydrodynamic models", Computers and Geosciences, 2011.

[9] R.A. Olea, "Geostatistics for engineers and earth scientists", Norwell, Massachussetts 02061 USA, p. 303, 2003.

[10] B. Jeanty-Ruard, B. Thiebault, « Documentation sur l'évolution des algorithmes d'interpolation », Ifremer BMGTools Project, internal technical documentation, contract ref. 12/2.212.883, 2012.

[11] G. Heiken, D. Vaniman, B.M. French (Eds.). "Lunar sourcebook: A user's guide to the Moon", Cambridge University Press, 1991.

[12] R.F. Willis, M. Anderegg, B. Feuerbacher, B. Fitton, "Photoemission and Secondary Electron Emission from Lunar Surface Material", 6th ESLAB Symposium, Noordwijk, 1972, edited by R.J.L. Grard. Astrophysics and Space Science Library, Vol. 37, p.389, 1973.

[13] V.W. Chow, D. A. Mendis, M. Rosenberg, "Role of grain size and particle velocity distribution in secondary electron emission in space plasmas", J. Geophys. Res., 98(A11), p. 19065–19076, 1993.

[14] A. Poppe, M. Horányi, "Simulations of the photoelectron sheath and dust levitation on the lunar surface", J. Geo. Res., 115, A08106, 2010.

[15] S. Dyadechkin, E. Kallio,P.Wurz,"New fully kinetic model for the study of electric potential, plasma and dust above lunar landscapes", J. Geo. Res., In Press, 2015

[16] S. L. G. Hess, P. Sarrailh, J. C. Matéo-Vélez, F. Cipriani, S.R. Marple, F. Honary, V. Inguimbert, "Modeling of the photoelectron sheath above thecratered lunar surface and its variation with solar inclination and environments", Planetary and Space Science, submitted, 2015

[17] D.W. Strangway, W.B. Chapman, G.R. Olhoeft, J. Carnes, "Electrical properties of lunar soil dependence on frequency, temperature and moisture", Earth and Planetary Science Letters, Vol. 16, Issue 2, 275–281, 1972

[18] H. Perko, J. Nelson, W. Sadeh,"Surface Cleanliness Effect on Lunar Soil Shear Strength." J. Geotech. Geoenv. Eng., 127(4), p. 371–383, 2001.

[19] A.R. Dove, "Experimental investigations of the lunar photoelectron environment and related dust dynamics," Univ. of Colorado, USA, 2012.

[20] C.M. Hartzell, D.J. Scheeres, "Dynamics of levitating dust particles near asteroids and the Moon", J. Geophys. Res. Planets, 118, 116–125, 2013.

[21] Z. Sternovsky, S. Robertson, A. Sickafoose, J. Colwell, et M. Horányi, "Contact charging of lunar and Martian dust simulants", J.-Geophys.-Res., vol. 107, E11, p. 5105, nov. 2002.

[22] Whipple, E. C., T. G. Northrop, and D. A. Mendi, "The electrostatics of a dusty plasma", J. Geophys. Res., 90, 7405–7413, 1985.

[23] B. Feuerbacher, M. Anderegg, B. Fitton, L.D. Laude, R.F. Willis, R.J.L. Grard, "Photoemission from lunar surface fines and the lunar photoelectron sheath", Proceedings of the Lunar Science Conference, vol. 3, p.2655, 1972.

[24] A. R. Poppe, M. Piquette, A. Likhanskii, and M. Horányi, "The effect of surface topography on the lunar photoelectron sheath and electrostatic dust transport", Icarus, vol. 221, nº 1, p. 135‑146, sept. 2012.

[25] T. J. Stubbs, R. R. Vondrak, and W. M. Farrell, "A dynamic fountain model for lunar dust", *Advances in Space Research*, *37*(1), 59-66, 2006